PAPER

Check for updates

Atomic insight into the effects of precursor clusters on monolayer WSe$_2$†

Yanxue Zhang, Yuan Chang, Luneng Zhao, Hongsheng Liu [ID] * and Junfeng Gao [ID]

Two-dimensional (2D) transition metal dichalcogenides (TMDCs) have been attracting much attention due to their rich physical and chemical properties. At the end of the chemical vapor deposition growth of 2D TMDCs, the adsorption of excess precursor clusters onto the sample is unavoidable, which will have significant effects on the properties of TMDCs. This is a concern to the academic community. However, the structures of the supported precursor clusters and their effects on the properties of the prepared 2D TMDCs are still poorly understood. Herein, taking monolayer WSe$_2$ as the prototype, we investigated the structure and electronic properties of Se$_N$, W$_N$ (N = 1–8), and W$_{8-N}$Se$_N$ (N = 1–7) clusters adsorbed on monolayer WSe$_2$ to gain atomic insight into the precursor cluster adsorption. In contrast to W clusters that tightly bind to the WSe$_2$ surface, Se clusters except for Se$_1$ and Se$_2$ are weakly adsorbed onto WSe$_2$. The interaction between W$_{8-N}$Se$_N$ (N = 1–7) clusters and the WSe$_2$ monolayer decreases with the increase in the Se/W ratio and eventually becomes van der Waals interaction for W$_1$Se$_7$. According to the phase diagram, increasing the Se/W ratio by changing the experimental conditions will increase the ratio of Se$_N$ and W$_1$Se$_7$ clusters in the precursor, which can be removed by proper annealing after growth. W clusters induce lots of defect energy levels in the band gap region, while the adsorption of W$_1$Se$_7$ and Se$_N$ clusters (N = 3–6, 8) promotes the spatial separation of photo generated carriers at the interface, which is important for optoelectronic applications. Our results indicate that by controlling the Se/W ratio, the interaction between the precursor clusters and WSe$_2$ as well as the electronic properties of the prepared WSe$_2$ monolayer can be effectively tuned, which is significant for the high-quality growth and applications of WSe$_2$.

Key laboratory of Materials Modification by Laser, Ion and Electron Beams (Dalian University of Technology), Ministry of Education, Dalian, 116024, China.
E-mail: liuhongsheng@dlut.edu.cn
†Electronic supplementary information (ESI) available. See DOI: https://doi.org/10.1039/d3nr05562k

Hongsheng Liu obtained his PhD degree in condensed matter physics from the Dalian University of Technology in 2016. He is currently an associate professor in the Department of Physics at Dalian University of Technology. His research interests include structure and property tuning of nanomaterials and the applications of nanoclusters in nanomedicine.

Hongsheng Liu

Introduction

Two-dimensional (2D) layered transition metal dichalcogenides (TMDCs) belong to a large family that exhibit rich properties.[1–5] Compared to zero-gap graphenes, semiconducting TMDCs with proper bandgaps have attracted much attention.[6–10] Moreover, the band gap of these TMDCs is tunable *via* the number of layers and strain.[11–15] Monolayer WSe$_2$, a member of TMDCs, exhibits a typical sandwich structure, Se–W–Se, where the W atomic layer is surrounded by two Se atomic layers and can be mechanically exfoliated from the bulk WSe$_2$.[16–18] When the layer thickness of WSe$_2$ is reduced to monolayer, an indirect-to-direct band gap transition is observed.[19,20] WSe$_2$ has large exciton binding energies,[21–23] large carrier mobility,[24–26] and large absorption coefficients in the range of infrared to visible region,[27–29] which are promising in the field of photonics, optoelectronics, and photodetectors. In addition, WSe$_2$ has excellent catalytic performance.[30–33]

Surface-supported clusters have been extensively studied, as the interaction between clusters and substrates plays an important role in the performance of catalysts and the growth of 2D

materials.[34–43] For example, Au cluster depositions on a TiO_2 surface can effectively catalyze CO oxidation.[34,35] TiC-supported Ni clusters could capture and activate methane at room temperature.[38] Chen *et al.* studied 134 bare and compound clusters anchored on 2D N vacancy W_2N_3 (NV-W_2N_3) by high-throughput screening and proposed that VNiCu cluster-anchored NV-W_2N_3 shows the best performance for electro-catalytic nitrogen reduction reactions.[42] Theoretical calculations show that the interaction between phosphorene nanoflakes and substrates around 0.35 eV per P atom is moderate to maintain the 2D feature of the phosphorene nanoflake.[36] The cesium iodide cluster prefers to form on monolayer graphenes, while 2D CsI forms only on bilayer graphenes.[39] In addition, a multilayer reduced graphene oxide (rGO)-supported Co_4W_{18} cluster shows excellent catalytic performance for Li_2S deposition and oxidation and better for Li–S batteries.[40] Zhang *et al.* theoretically investigated the structure and electronic properties of Li_2S_n cluster adsorption on various 2D materials and revealed that a suitable interaction between the Li_2S_n cluster and anchor materials can enhance the performance of Li–S batteries.[44] The post-synthesis strategies by incorporating excess Mo into $MoTe_2$ and $MoSe_2$ can modify the phase structure and electronic properties.[45]

The high-quality synthesis of WSe_2 is a prerequisite for its application. Chemical vapor deposition is the most common method for synthesizing WSe_2.[46–48] The selenium/tungsten (Se/W) ratio plays an essential role in the growth of monolayer WSe_2 and determines the type of precursor clusters. For example, Yue *et al.* proposed a high Se/W ratio, and an elevated substrate temperature is better for the growth of monolayer WSe_2.[49] Li *et al.* realized the precise control of hetero-epitaxy direction by manipulating the metal/chalcogenide ratio.[50] The theoretical calculations showed that at a high Se/W ratio, W_1Se_3 clusters are the dominant species in the growth process, and the diffusion barrier of W_1Se_3 clusters of only 0.4 eV promotes the growth along the in-plane direction.[50] In contrast, in a low Se/W ratio atmosphere, the components of W_1Se_x (x = 1–3) coexist, and W_1Se_1 clusters have a large diffusion barrier of about 1.2 eV, which can act as a nucleation site favorable for the growth along the out-of-plane direction.[50]

At the end of the chemical vapor deposition growth of 2D TMDCs, the adsorption of excess precursor clusters on the sample is unavoidable. As discussed above, these precursor clusters will have significant effects on the properties of TMDCs. However, the structures of the supported precursor clusters and their interaction with the 2D TMDCs as well as the effects on the properties of the prepared 2D TMDCs are still poorly understood.

In this work, we systematically investigated the structures of WSe_2-supported possible precursor clusters including Se_N, W_N (N = 1–8) and $W_{8-N}Se_N$ (N = 1–7) as well as their influence on the electronic properties of WSe_2 monolayer using first-principles calculations. The interaction between precursor clusters and the WSe_2 monolayer strongly depends on the Se/W ratio. By tuning the Se/W ratio, WSe_2 with weakly adsorbed precursor clusters can be obtained, and the precursor clusters are

expected to be removed by proper annealing. Interestingly, weakly adsorbed precursor clusters (W_1Se_7 and Se_N clusters (N = 3–6, 8)) will promote the spatial separation of photo generated carriers at the interface, which is important for optoelectronic applications. W clusters will tightly bind to the WSe_2 surface and induce lots of defect energy levels in the band gap region. Our results provide an atomic insight into the precursor cluster adsorption on the WSe_2 monolayer, which is significant for the high-quality growth and applications of WSe_2.

Computational methods

Following previous works, the ground-state structure of bare W_N or Se_N (N = 1–8) clusters in vacuum was constructed manually. The possible structure of $W_{8-N}Se_N$ (N = 1–7) clusters was searched using a self-developed comprehensive genetic algorithm (CGA) code implemented in the DMol^3 program,[51,52] which has been proved to be a reliable and powerful tool for cluster structure search.[52] The $W_{8-N}Se_N$ (N = 1–7) clusters were optimized using the double numerical basis including d-polarization function (DND) and the Perdew, Burke and Ernzerhof (PBE) functional within the generalized gradient approximation (GGA).[53] There are no symmetry constraints in the structure optimization. The number of maximum iterations of each search is set to 3000, and 16 members are retained in the population.

Vienna *Ab initio* Simulation Package (VASP)[54] can handle the problem of cluster adsorption on the surface well and give results that are in good agreement with the experiments. For example, by investigating the differences in the structure and stability of carbon clusters of adjacent sizes using DFT calculations with the VASP code, the branched C_{21}-3C clusters were proposed to have special stability on the Ru/Rh surface, revealing the true structure of the experimentally observed dominant clusters.[55,56] By investigating boron clusters on the Cu(111) surface using DFT calculations with the VASP, Liu and co-workers predicted the growth mechanism of borophene on a metal surface,[57] which was confirmed by later experiments.[58,59] Recently, combining experiments and VASP theoretical calculations, Zhou and co-workers investigated the growth mechanism of 67 types of transition metal chalcogenides (TMCs) and transition metal phosphorous chalcogenides (TMPCs) on a silicon substrate.[60] The calculations regarding the chemical transition between different phases of TMCs well matched the experimental observation. Therefore, for the study of $W_{8-N}Se_N$ (N = 0–8) clusters on the WS_2 monolayer layer, we adopted the VASP code.

The searched $W_{8-N}Se_N$ (N = 1–7) cluster structure is then further optimized using the VASP code. The structure and electronic properties of the bare W_N or Se_N (N = 1–8) cluster and the composite $W_{8-N}Se_N$ (N = 1–7) cluster adsorption on the monolayer WSe_2 were studied by spin-polarized density functional theory (DFT) calculations implemented in the VASP. The GGA-PBE was used to tackle the exchange and correlation

functional. The electron-ion interactions were described by the projector augmented wave (PAW) potentials.[61] The Grimme scheme DFT-D3 with a Becke–Jonson damping approach was used to describe the van der Waals (vdW) interactions between the cluster and the substrate.[62,63] A vacuum space larger than 20 Å along the z-direction was set to avoid the interactions between the periodic replicas. The energy cutoff of the plane wave basis set was 500 eV. The Monkhorst–Pack k-point mesh with a separation of 0.02 Å^{-1} was used to sample the Brillouin zones.[64] All atoms were relaxed and the lattice was fixed. The total energy convergence criterion was 10^{-5} eV and the force convergence criterion was 0.01 eV Å^{-1}. The diffusion barrier of a single W or Se atom on the monolayer WSe$_2$ surface was simulated by the climbing-image nudged elastic band (CI-NEB) method.[65,66] Four images were used to simulate the diffusion path. The charge transfer between the cluster and the monolayer WSe$_2$ surface was obtained by Bader charge analysis.[67] The simulated scanning tunneling microscopic (STM) images were obtained using the Tersoff–Hamann approximation.[68] The distance from the surface was kept constant, and the details are listed in Table S1.†

Results and discussion

Before investigating the structures of WSe$_2$-supported W$_N$, Se$_N$ (N = 1–8) and W$_{8-N}$Se$_N$ (N = 1–7) clusters, the primitive cell of monolayer WSe$_2$ is fully relaxed. The calculated equilibrium lattice constant of monolayer WSe$_2$ is 3.316 Å, which is in good agreement with the previous theoretical results.[69–72] We then transformed the primitive cell of WSe$_2$ into the orthogonal unit cell and created a (5 × 3) supercell, as shown in Fig. S1.† The lattice constants of the (5 × 3) supercell of WSe$_2$ are 16.58 Å and 17.229 Å along the x- and y-directions, respectively. Such a dimension of the supercell is expected to sufficiently avoid the interactions between periodic replicas.

We first studied the adsorption of a single W atom on the perfect WSe$_2$ surface. Here, we consider three adsorption sites, including the top of the W atom (T$_W$), the top of the Se atom (T$_{Se}$) and the hollow (H) site, as shown in Fig. S1.† By comparing the total energy of the three adsorption sites, the most stable adsorption site of the single W atom on the monolayer WSe$_2$ surface was obtained, i.e. the W atom prefers to adsorb on the T$_W$ site of the monolayer WSe$_2$ surface, as shown in Fig. S2a† and Fig. 1a. Our results agree well with the previous study that the W atom prefers the T$_W$ site of the WSe$_2$ surface, which verifies the accuracy of our work.[73] In addition, we considered the possible configurations that the W single atom was buried within the WSe$_2$ layer, as shown in Fig. S2d and e.† The W atom buried within the WSe$_2$ layer can significantly reduce the energy and the configuration of the W atom embedded at the T$_W$ site has the lowest energy, which is in agreement with the result reported by Zheng et al.[74] This phenomenon is very interesting and additional energy must be needed to trigger this process. In this paper, we will not consider the burial of

W atoms, leaving the discussion of the formation mechanism in our next work.

We then investigated the possible adsorption configuration of W$_N$ (N = 2–8) clusters on monolayer WSe$_2$. For each size, several different structures are constructed to find out the most stable one, as shown in Fig. S3–S9 in the ESI.† After geometry optimization, the most stable structures for W$_N$ (N = 1–8) are shown in Fig. 1a. For the W$_2$ cluster on the WSe$_2$ monolayer, the most stable configuration is that one W atom is set on the T$_{Se}$ site of the WSe$_2$ surface and the other W atom is set on the hollow site and binds with two Se atoms. For the W$_3$ cluster, after structure optimization, the linear W$_3$ cluster is reconstructed into the triangle W$_3$ cluster, which is the most stable configuration of W$_3$ cluster adsorption on the monolayer WSe$_2$ surface. Two W atoms of the W$_3$ cluster bind with Se atoms on the surface with one W atom at the T$_W$ site and the other W atom at the T$_{Se}$ site. For W$_4$ on WSe$_2$, the most stable configuration is a tetrahedral W$_4$ cluster with two W atoms at the T$_W$ site binding with Se atoms on the surface. The result indicates that the linear configuration is not favorable for the W$_4$ cluster on the WSe$_2$ surface. Therefore, we ignore linear clusters for larger W clusters. The stable W$_5$ cluster is a pentahedral with two W atoms chemically binding with Se atoms on the surface. The W$_6$ cluster prefers a triangular antiprism structure with three W atoms binding with Se atoms. For W$_7$ and W$_8$ clusters on the surface, four W atoms bind with Se atoms on the surface.

The ground state structure of bare W$_N$ (N = 1–8) clusters in vacuum has been widely studied theoretically, which is also optimized in this work, as shown in Fig. S10.†[75,76] The calculated bond length of the W$_2$ cluster is 1.860 Å, which is in agreement with the previous study, 1.835 Å.[76] The structure of the free-standing W$_3$ cluster is equilateral triangle with a bond length of 2.235 Å. For the size larger than 3, all the structures of the free-standing W cluster show 3D geometries. For example, the W$_4$ cluster is a tetrahedron, the W$_5$ cluster is a distorted trigonal bipyramid, and the W$_7$ cluster is a distorted pentagonal bipyramid. Compared with Fig. 1a and Fig. S10,† we can see that the W$_N$ (N = 4–8) cluster is preferred to form 3D configuration irrespective of whether in vacuum or on substrate, which indicates that the W atom on the substrate showed consistent behavior with that in vacuum. However, the most stable configuration is slightly different from that in vacuum. For example, for the W$_2$ cluster, the bond length of the W–W bond is 1.940 Å, slightly longer than that in vacuum by about 0.08 Å. For the W$_3$ cluster, the shape of the W$_3$ cluster on the WSe$_2$ surface is distorted from equilateral triangle to irregular triangle with bond lengths of 2.134 Å, 2.414 Å and 2.317 Å, respectively. The bond lengths of the W–W bond in the W$_4$ cluster are stretched from 2.540 Å to 2.839 Å. The minimum atomic distance between the W$_N$ (N = 1–8) cluster and the substrate is also marked in Fig. 1a. The single W atom has the smallest relative minimum atomic distance, 1.58 Å. The W$_8$ cluster has the largest relative minimum atomic distance, 2.30 Å. The relative minimum atomic distance between W$_N$ (N = 2–7) clusters and the substrate is in the range of
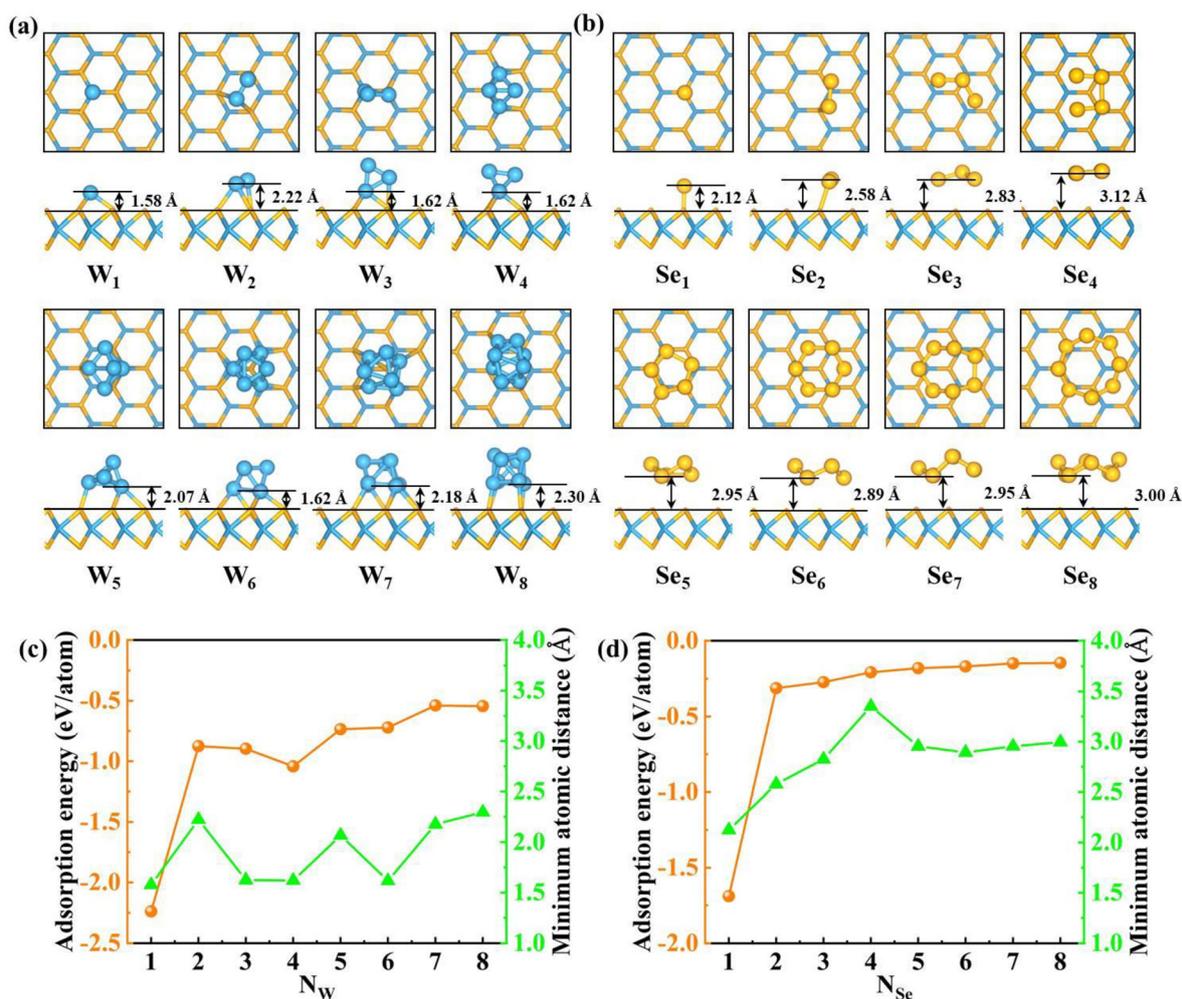
Fig. 1 Top and side views of (a) W_N (N = 1–8) and (b) Se_N (N = 1–8) cluster adsorption on the monolayer WSe_2 surface. The blue and orange spheres indicate W and Se atoms, respectively. For the sake of clarity, the substrate is shown as a stick. The adsorption energy of (c) W_N (N = 1–8) and (d) Se_N (N = 1–8) clusters on the substrate (yellow line) and the minimum atomic distance between clusters and the substrate (green line).

1.58 Å–2.30 Å. To evaluate the possibility of cluster formation on the WSe_2 surface, the formation energy is defined as follows:

$$E_f = (E_{total} - E_{sub} - N \times E_X)/N,$$

where E_{total} and E_{sub} are the total energies of the absorbed system and bare monolayer WSe_2 substrate, respectively. E_X is the energy per atom in bulk W or Se, The subscript X represents element W or Se. N is the number of atoms in the W_N or Se_N cluster.

The formation energy of W_N clusters in vacuum and on substrate is plotted in Fig. S11.† As the size increases, the formation energy gradually decreases. For supported W_N (N = 1–8) clusters, the formation energy has a similar trend as in vacuum, but always lower in energy, indicating that the WSe_2 monolayer can stabilize W_N (N = 1–8) clusters. Larger W clusters have lower formation energies than those of smaller W clusters. Therefore, we investigated the energy barrier of single W atom diffusion on the WSe_2 surface to form large W clus-

ters, as shown in Fig. S12.† The initial state (IS) is set as two W atoms adsorbed on the two separate T_W sites. In addition, the final state (FS) is a W_2 cluster. As shown in Fig. S12,† the W_2 cluster adsorption configuration is more stable than the configuration of the two separate W atoms. The calculated energy barrier of W atom diffusion on the WSe_2 surface is 0.62 eV, and the small atom diffusion barrier indicates that the W atom is easy to diffuse, which implies that *via* W atom diffusion into the WSe_2 surface, growing large W cluster is more feasible. The corresponding transition state (TS) is shown in Fig. S12c,† where a W atom is moved from the T_W site to the nearby T_{Se} site.

We then calculated the adsorption energy of the W_N clusters on the monolayer WSe_2 surface. The adsorption energy is defined as follows:

$$E_{ads} = (E_{total} - E_{sub} - E_{X_N})/N$$

where E_X is the energy of the X_N cluster, X is W or Se. The adsorption energy of W_N (N = 1–8) clusters on the WSe_2 mono-

layer is shown in Fig. 1c. From this, we can see that the adsorption energy of W_N (N = 1–8) clusters on the WSe$_2$ surface is below zero, indicating that the surface favors the adsorption of W_N (N = 1–8) clusters. Among them, the single W atom has the largest adsorption energy, −2.24 eV per atom. In general, the adsorption energy gradually decreases with the increase in size, and the minimum atomic distance increases with the size of the cluster. It can be expected that the inter-cluster atomic interaction is stronger than the cluster-substrate interaction as the size increases.

Furthermore, the projected band structures of monolayer WSe$_2$ with W_N (N = 1–8) clusters on the surface were calculated (Fig. S13†). Compared to the pristine WSe$_2$ monolayer, W_N clusters induce many impurity states in the gap region. The Fermi level is close to the CBM, indicating that W clusters transfer electrons to the WSe$_2$ monolayer and make the monolayer n-doped. In addition, the W_1, W_5 and W_8 clusters will induce spin polarization (as shown in Fig. S13a, e and h†).

Next, we begin to investigate the structure of Se$_N$ (N = 1–8) cluster adsorption on the WSe$_2$ surface. For single Se atoms, we consider five configurations, as shown in Fig. S14a–e.† The most favorable adsorption site is the T$_{Se}$ site (Fig. 1b), which is consistent with the previous results.[77] In contrast with the W atom, the configuration with the Se atom embedded in the WSe$_2$ layer is very high in energy.

For Se$_N$ (N = 2–8) clusters on monolayer WSe$_2$, several different structures are constructed for each size to find out the most stable one, as shown in Fig. S15–S21 in the ESI.† After geometry optimization, the most stable structures for Se$_N$ (N = 1–8) are shown in Fig. 1b. For the Se$_2$ cluster on the WSe$_2$ monolayer, the most stable configuration is a Se dimer with one Se atom chemically bonded with one Se atom on the surface. When N > 2, no chemical bond appears at the Se$_N$ cluster/WSe$_2$ interface. For Se$_5$, Se$_6$, Se$_7$ and Se$_8$, five-, six-, seven- and eight-membered rings are the most stable configurations.

The Se vapor is predominantly Se$_N$ (N < 8) cluster, as indicated by the mass spectra.[78] Subsequently, the structure of the free-standing Se$_3$ to Se$_8$ clusters was theoretically calculated.[79,80] We reproduced the previously predicted structure of free-standing Se$_N$ (N = 3–8), as shown in Fig. S22.† The structure of free-standing Se$_3$ and Se$_4$ clusters is an open triangular structure and an open planar tetragonal structure, respectively. From Se$_5$ to Se$_8$ clusters, the structure is buckled pentagon, hexagon, heptagon and octagon ring, respectively. Compared with the structure of the Se$_2$ cluster in vacuum, the bond length of the Se–Se bond in the Se$_2$ cluster on the substrate is extended from 2.194 Å to 2.230 Å. For the Se$_3$ cluster, which is not bonded to the WSe$_2$ surface, the length of the Se–Se bond in the Se$_3$ cluster changed from two equal bond lengths of 2.228 Å to two unequal bond lengths of 2.292 Å and 2.251 Å, respectively, and the bond angle changed from 116.658° to 112.481°. Similar to the Se$_3$ cluster, the Se$_4$ cluster is not bonded to the substrate. The Se–Se bond in the Se$_4$ cluster can be divided into two types, namely, two equivalent short Se–Se bonds (2.187 Å) and one longer Se–Se bond

(2.785 Å). After adsorption on the WSe$_2$ surface, the bond length of the short bond increased to 2.191 Å, and the longer bond length decreased to 2.682 Å. For the Se$_5$ cluster, the length of the Se–Se bond slightly increased from 2.300 Å to 2.302 Å, 2.390 Å to 2.400 Å, and 2.387 Å to 2.391 Å, respectively. For the Se$_6$ cluster, the length of the Se–Se bond increased from 3.364 Å to 3.370 Å. For the Se$_7$ and Se$_8$ clusters, the length of the Se–Se bond changed by less than 0.005 Å. The single Se atom has the smallest minimum atomic distance, 2.12 Å. This is followed by the Se$_2$ cluster, 2.58 Å. The Se$_4$ cluster has the largest minimum atomic distance, 3.35 Å.

The formation energy of Se$_N$ (N = 1–8) clusters in vacuum is shown in Fig. S23.† It can be seen that as the cluster size increases, and the formation energy gradually decreases. The Se$_8$ cluster has the lowest formation energy of 0.26 eV per atom. The formation energy of Se$_N$ (N = 1–8) clusters on the monolayer WSe$_2$ surface has a similar trend with Se$_N$ (N = 1–8) clusters in vacuum, but it is always lower than that in vacuum, indicating that Se$_N$ (N = 1–8) clusters prefer to be deposited on the monolayer WSe$_2$ surface. Based on the formation energy of Se$_N$ (N = 1–8) clusters on the WSe$_2$ surface, we can conclude that large-sized clusters are easily formed on the WSe$_2$ surface. Therefore, the barrier of Se atom diffusion on the WSe$_2$ surface to form large clusters was investigated, as shown in Fig. S24.† The initial state is two Se atoms on separate T$_{Se}$ sites and the final state is set at the Se$_2$ cluster adsorption on the WSe$_2$ surface. On the WSe$_2$ monolayer, the Se$_2$ cluster is more stable than the two separate Se atoms and the energy barrier of Se atom diffusion is 1.02 eV. The high barrier indicates that it is difficult to form large Se clusters by the diffusion of single Se atoms on the surface and that the direct deposition of the vapor large Se clusters on the surface is practical.

The adsorption energy of Se$_N$ (N = 1–8) clusters on the WSe$_2$ monolayer is shown in Fig. 1d, from which we can see that the single Se atom has the largest adsorption energy (−1.69 eV per atom). The adsorption energy of Se$_2$ to Se$_8$ clusters is in the range of −0.14 to −0.31 eV per atom. Compared to W_N (N = 1–8) clusters, Se$_N$ (N = 1–8) clusters have weaker interaction with the substrate. The minimum atomic distance between the Se$_N$ (N = 1–8) cluster and the substrate increases with the increase in cluster size, and is always greater than that between the W_N (N = 1–8) cluster and the substrate. Especially, the interaction between Se$_N$ (N = 3–8) clusters and the WSe$_2$ monolayer is weak vdW interaction, indicating their ease of removal under proper annealing.

To check the effect of Se$_N$ (N = 1–8) cluster adsorption on the electronic properties of WSe$_2$, the projected band structures are plotted (shown in Fig. S25†). In general, few defects are induced in the band gap region, which is in sharp contrast with the case of W clusters. According to the location of the highest occupied molecular orbital (HOMO) and lowest unoccupied molecular orbital (LUMO) orbits of the Se$_N$ clusters, Se$_N$ clusters (N = 3–6, 8) would promote the spatial separation of photo generated carriers at the interface. The high efficiency charge separation is a key factor affecting the photocatalytic performance of semiconductors.[81–87] For example, charge sep-

aration greatly improves the efficiency of CO_2 photo-reduction and hydrogen evolution reactions.[81,87] Therefore, the Se_N (N = 3–6, 8) cluster deposition on the WSe_2 surface provided an atomic level strategy to promote charge separation, which is important for optoelectronic applications.

For convenient experimental observation of the clusters, the scanning tunneling microscopic (STM) images of W_N and Se_N (N = 1–8) clusters are simulated and shown in Fig. 2. In general, the adsorbed W_N clusters appear as a big bright point in the STM image, and the larger the cluster, the larger the bright point. For Se_N clusters, they also appear as bright points and the patterns in STM images are more recognizable. For example, the Se_2 cluster shows as a bone-like pattern and the Se_8 cluster appears as an eight-membered ring.

To further illustrate the cluster-substrate interaction, the charge density difference and the corresponding Bader charge transfer between the clusters and the WSe_2 monolayer are plotted, as shown in Fig. 3. The results show that W_N (N = 1–8) clusters transfer electrons to the WSe_2 monolayer, resulting in n-type doping of the monolayer WSe_2. Se_N (N = 1–4) clusters

gain electrons from the WSe_2 layer, while Se_5 slightly transfers electrons to the WSe_2 layer. For Se_6, S_7 and Se_8 clusters, there is almost no electron transfer between clusters and the WSe_2 layer. The less charge transfer between Se_N clusters and the WSe_2 layer again confirms the weak interaction at the interface which is in sharp contrast to W_N clusters.

In experiments, the selenium/tungsten (Se/W) ratio has a strong influence on the growing monolayer WSe_2.[50,88,89] Using the self-developed CGA software,[52] several low-energy $W_{8-N}Se_N$ (N = 1–7) binary clusters in vacuum were determined (shown in Fig. S26–S32†). The detailed discussion about the ground state (GS) structures of free-standing $W_{8-N}Se_N$ (N = 1–7) binary clusters can be found in the ESI.† Subsequently, these searched $W_{8-N}Se_N$ (N = 1–7) binary clusters were put on the WSe_2 monolayer (shown in Fig. S33–S39†) to investigate supported $W_{8-N}Se_N$ (N = 1–7) binary clusters. The most stable structures of the WSe_2-supported $W_{8-N}Se_N$ (N = 1–7) binary clusters are shown in Fig. 4a. In comparison, the WSe_2 substrate has a great influence on the geometry of the compound clusters. For example, compared to the free-standing GS W_7Se_1
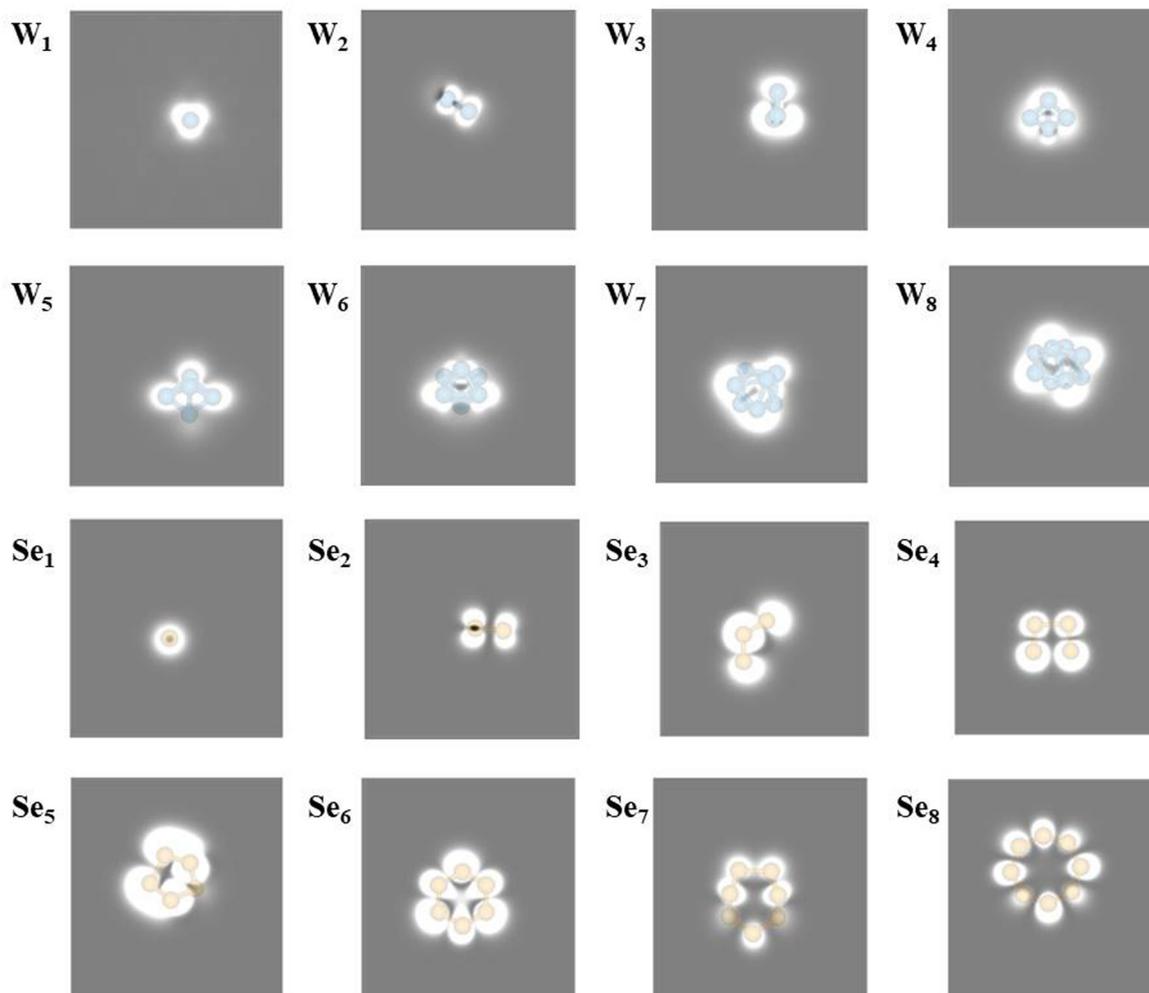

Fig. 2 Simulated STM of W_N (N = 1–8) and Se_N (N = 1–8) cluster adsorption on the WSe_2 surface at −0.6 V bias, respectively.
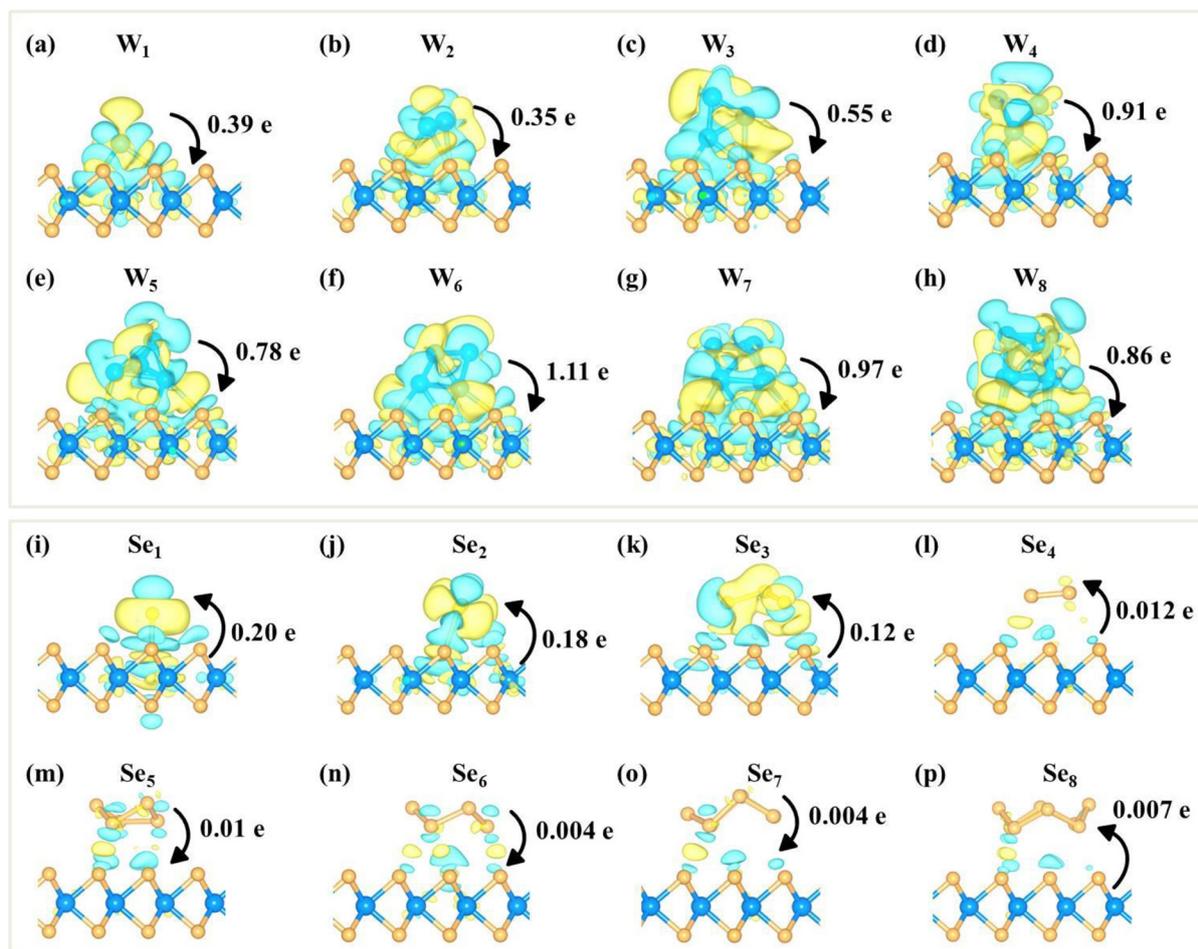
Fig. 3 Charge density difference of (a–h) W_N (N = 1–8) and (i–p) Se_N (N = 1–8) clusters adsorbed on the WSe_2 surface. The accumulation and depletion of charge density are represented in yellow and green colors. The value and direction of the Bader charge transfer are also marked. The isosurface value is 0.0005 e Bohr^{-3}.

cluster, the supported GS W_7Se_1 cluster is distorted. The metastable W_1Se_7 cluster in vacuum (Fig. S32b†) becomes the most stable one when adsorbed on the surface (Fig. 4a). When the Se/W ratio is less than 7, the $W_{8-N}Se_N$ (N = 1–6) clusters prefer to bond with the surface through W-Se chemical bonds. Therefore, $W_{8-N}Se_N$ (N = 1–6) interact strongly with the WSe_2 surface. As the Se/W ratio increases, the number of chemical bonds at the interface decreases. When the Se/W ratio reaches 7, the minimum atomic distance between the cluster and the WSe_2 substrate increases from 1.64 Å to 3.02 Å and no chemical bonds exist at the interface. The W_1Se_7 clusters prefer physical adsorption on the WSe_2 surface. Therefore, by tuning the Se/W ratio, the interaction between $W_{8-N}Se_N$ and the WSe_2 layer can be effectively tuned.

The charge density difference and the corresponding Bader charge transfer between the $W_{8-N}Se_N$ (N = 1–7) cluster and the WSe_2 surface are shown in Fig. 4 to reveal the interaction between the cluster and the substrate. When the number of Se atoms increases from 1 to 7, there is almost no electron transfer between the cluster and the substrate. The W_1Se_7 cluster

transfers only 0.014 e to the substrate, again indicating the weak interaction between the W_1Se_7 clusters and the substrate. The $W_{8-N}Se_N$ (N = 1–4) cluster donates electrons to the substrate, resulting in an n-type WSe_2 monolayer, while the $W_{8-N}Se_N$ (N = 5, 6) cluster accepts electrons from the substrate resulting in a p-type WSe_2 monolayer. For W_1Se_7, there is almost no charge transfer.

For W_N and Se_N (N = 1–8) clusters, W_8 and Se_8 are the most stable on the WSe_2 monolayer. To estimate the stability of binary $W_{8-N}Se_N$ (N = 1–7) clusters, we constructed the phase diagram of W_8, Se_8 and $W_{8-N}Se_N$ (N = 1–7) clusters on the substrate based on the chemical potential of W and Se atoms. The formation energy of $W_{8-N}Se_N$ (N = 1–7) clusters as a function of W chemical potential (μ_W) and Se chemical potential (μ_{Se}) is defined as follows:

$$E_f = E_{total} - E_{sub} - (8 - N) \times \mu_W - N \times \mu_{Se},$$

where E_{total} and E_{sub} are as defined above. N is the number of Se atoms in the $W_{8-N}Se_N$ (N = 1–7) cluster. In Fig. 5, nine stable phases are determined, marked by different colors. In
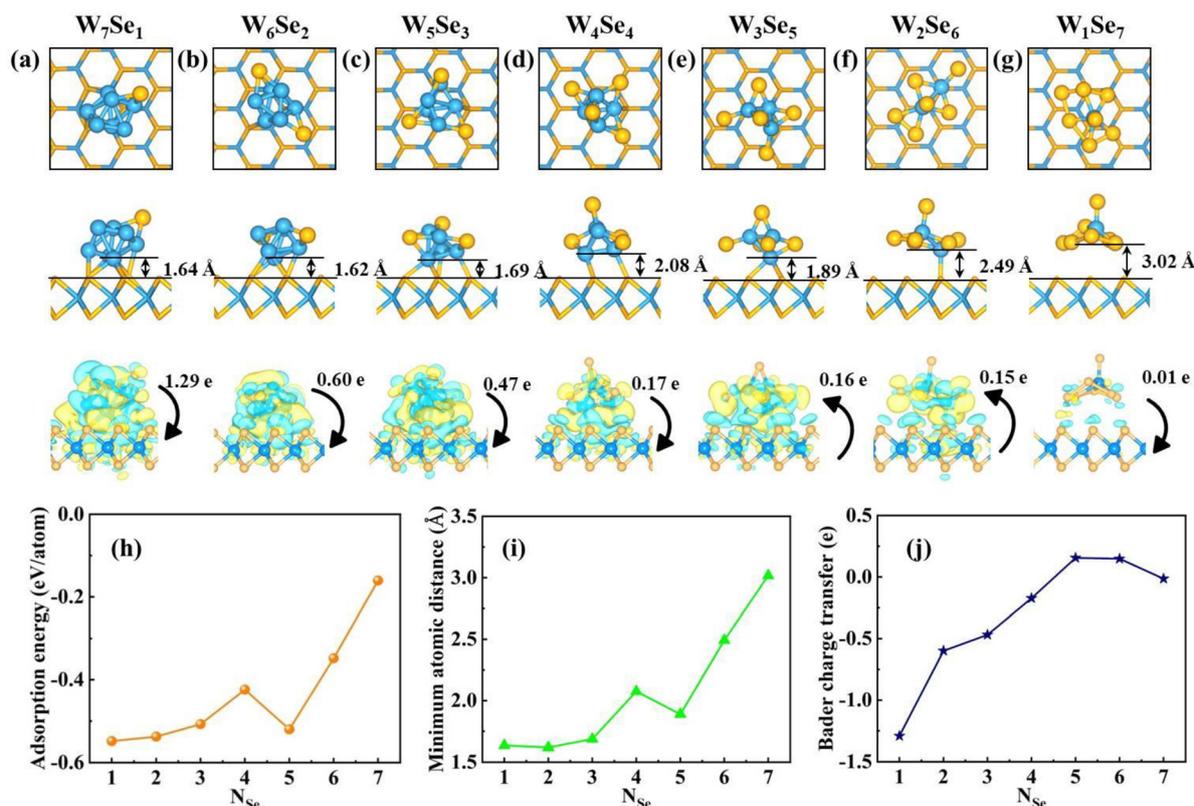
Fig. 4 Top and side views of (a–g) $W_{8-N}Se_N$ (N = 1–7) cluster adsorption on the monolayer WSe_2 surface, the minimum atomic distance, charge density difference and corresponding Bader charge transfer. (h) Adsorption energy of $W_{8-N}Se_N$ (N = 1–7) cluster adsorption on the monolayer WSe_2 surface. (i) Minimum atomic distance of $W_{8-N}Se_N$ (N = 1–7) cluster adsorption on the monolayer WSe_2 surface. (j) Bader charge transfer of $W_{8-N}Se_N$ (N = 1–7) cluster adsorption on the monolayer WSe_2 surface. The negative value of the Bader charge transfer indicates that the cluster loses electrons and the positive value of the Bader charge transfer indicates that the cluster gains electrons.
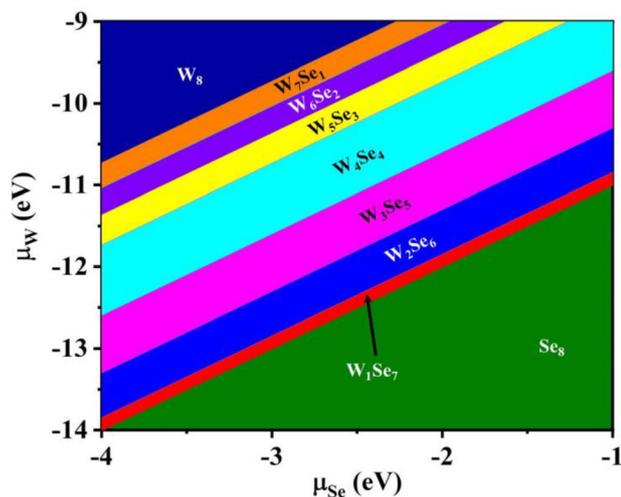

Fig. 5 Phase diagram of bare W_8, Se_8 and compound $W_{8-N}Se_N$ (N = 1–8) clusters adsorbed on the WSe_2 surface.

experiments, by tuning μ_{Se} and μ_W in an appropriate range, the desired phase could be formed. For example, if μ_{Se} is −1 eV and μ_W is in the range of −10 to −9 eV, the W_3Se_5 cluster could

be formed on the WSe_2 surface. The STM images of the $W_{8-N}Se_N$ (N = 1–7) cluster are also simulated, as shown in Fig. S40.† The simulated STM image is more complicated than the W_N and Se_N (N = 1–8) clusters.

The projected band structures of the WSe_2 monolayer with $W_{8-N}Se_N$ (N = 1–8) clusters on it are also examined, as shown in Fig. S41.† At a low Se/W ratio (N < 7), $W_{8-N}Se_N$ clusters will induce many impurity states in the gap region like W_N clusters. For the W_1Se_7 cluster, the LUMO and HOMO of the W_1Se_7 cluster are staggered with the valence band maximum (VBM) and conduction band minimum (CBM) of WSe_2, implying that the W_1Se_7 cluster and WSe_2 monolayer surface form a type-II band alignment, which will promote the spatial separation of photo generated carriers at the interface.

Briefly, among the W_N, Se_N (N = 1–8) and $W_{8-N}Se_N$ (N = 1–7) clusters, Se_N (N = 3–8) and W_1Se_7 clusters have low adsorption energy on the WSe_2 surface, which are more easily removed from the surface to form clean monolayer WSe_2. In addition, cluster adsorption on the WSe_2 surface is an effective tool to modify the electronic properties of WSe_2. The Se_N (N = 3–6,8) and W_1Se_7 cluster adsorption could form a unique type-II band alignment. W_N (N = 1–8) and $W_{8-N}Se_N$ (N = 1–7) clusters induced a large number of impurity states in the band gap

region of the pristine WSe$_2$ monolayer. In this work, the dynamic process of cluster transition from W$_7$Se$_1$ to W$_1$Se$_7$ and the specific temperature needed to remove Se$_N$ clusters by annealing were not considered. The effect of the presence of hydrogen on the structure was also not considered. There are also interesting and important issues to be discussed and they are left to be solved in our next work.

Conclusions

In summary, the adsorption of possible precursor clusters W$_N$ and Se$_N$ (N = 1–8) as well as W$_{8-N}$Se$_N$ (N = 1–7) on monolayer WSe$_2$ was carefully investigated using first-principles calculations. The GS structures for these clusters in vacuum and on the WSe$_2$ layer were well studied. The interaction between W$_N$ clusters and the WSe$_2$ layer is very strong, so that it is hard to remove W$_N$ clusters. In contrast, the interaction between Se$_N$ clusters and the WSe$_2$ layer is weak vdW interaction except for single Se atoms and Se dimers. The interaction between W$_{8-N}$Se$_N$ and the WSe$_2$ layer depends on the Se/W ratio. A high Se/W ratio (N = 7) results in weak interaction at the interface, while low Se/W (N < 7) results in W–Se chemical bonds at the interface. The stability of W$_N$ and Se$_N$ (N = 1–8) as well as W$_{8-N}$Se$_N$ (N = 1–7) on monolayer WSe$_2$ is related to the chemical potential of W and Se and the phase diagram is plotted. Increasing the Se/W ratio by changing the experimental conditions would increase the ratio of Se$_N$ and W$_1$Se$_7$ clusters in the precursor clusters, which can be removed by proper annealing. Moreover, W$_N$ clusters induce many defect states in the band gap region. Se$_N$ (N = 3–6, 8) and W$_1$Se$_7$ clusters will promote the spatial separation of photo generated carriers at the interface, due to the alignment of HOMO and LUMO of the clusters with the VBM and CBM of the WSe$_2$ monolayer. This spatial separation is important for optoelectronic applications. Our results provide an atomic insight into the precursor clusters adsorbed on the WSe$_2$ monolayer. We suggest that the interaction between the precursor clusters and the WSe$_2$ monolayer as well as the electronic properties of the prepared WSe$_2$ monolayer can be tuned by controlling the Se/W ratio, which is significant for the high-quality growth and applications of WSe$_2$.

Conflicts of interest

The authors declare no competing financial interest.

Acknowledgements

References

1   Q. H. Wang, K. Kalantar-Zadeh, A. Kis, J. N. Coleman and M. S. Strano, *Nat. Nanotechnol.*, 2012, **7**, 699–712.
2   S. Manzeli, D. Ovchinnikov, D. Pasquier, O. V. Yazyev and A. Kis, *Nat. Rev. Mater.*, 2017, **2**, 17033.
3   Z. Hu, Z. Wu, C. Han, J. He, Z. Ni and W. Chen, *Chem. Soc. Rev.*, 2018, **47**, 3100–3128.
4   X. Wu, H. Zhang, J. Zhang and X. W. Lou, *Adv. Mater.*, 2021, **33**, 2008376.
5   T. Heine, *Acc. Chem. Res.*, 2014, **48**, 65–72.
6   A. K. Geim, *science*, 2009, **324**, 1530–1534.
7   C. H. Lui, L. Liu, K. F. Mak, G. W. Flynn and T. F. Heinz, *Nature*, 2009, **462**, 339–341.
8   J. Kang, S. Tongay, J. Zhou, J. Li and J. Wu, *Appl. Phys. Lett.*, 2013, **102**, 012111.
9   K. F. Mak, D. Xiao and J. Shan, *Nat. Photonics*, 2018, **12**, 451–460.
10 K. F. Mak and J. Shan, *Nat. Photonics*, 2016, **10**, 216–226.
11 C.-H. Chang, X. Fan, S.-H. Lin and J.-L. Kuo, *Phys. Rev. B: Condens. Matter Mater. Phys.*, 2013, **88**, 195420.
12 R. Frisenda, M. Drüppel, R. Schmidt, S. Michaelis de Vasconcellos, D. Perez de Lara, R. Bratschitsch, M. Rohlfing and A. Castellanos-Gomez, *npj 2D Mater. Appl.*, 2017, **1**, 10.
13 C. Hsu, R. Frisenda, R. Schmidt, A. Arora, S. M. Vasconcellos, R. Bratschitsch, H. S. J. Zant and A. Castellanos-Gomez, *Adv. Opt. Mater.*, 2019, **7**, 1900239.
14 L. Mennel, M. Paur and T. Mueller, *APL Photonics*, 2019, **4**, 034404.
15 F. Carrascoso, H. Li, R. Frisenda and A. Castellanos-Gomez, *Nano Res.*, 2020, **14**, 1698–1703.
16 H. Li, G. Lu, Y. Wang, Z. Yin, C. Cong, Q. He, L. Wang, F. Ding, T. Yu and H. Zhang, *Small*, 2013, **9**, 1974–1981.
17 H. Li, J. Wu, Z. Yin and H. Zhang, *Acc. Chem. Res.*, 2014, **47**, 1067–1075.
18 Q. Cheng, J. Pang, D. Sun, J. Wang, S. Zhang, F. Liu, Y. Chen, R. Yang, N. Liang, X. Lu, Y. Ji, J. Wang, C. Zhang, Y. Sang, H. Liu and W. Zhou, *InfoMat*, 2020, **2**, 656–697.
19 W. Zhao, Z. Ghorannevis, L. Chu, M. Toh, C. Kloc, P.-H. Tan and G. Eda, *ACS Nano*, 2013, **7**, 791–797.
20 H. Sahin, S. Tongay, S. Horzum, W. Fan, J. Zhou, J. Li, J. Wu and F. M. Peeters, *Phys. Rev. B: Condens. Matter Mater. Phys.*, 2013, **87**, 165409.
21 K. He, N. Kumar, L. Zhao, Z. Wang, K. F. Mak, H. Zhao and J. Shan, *Phys. Rev. Lett.*, 2014, **113**, 026803.
22 Y. You, X.-X. Zhang, T. C. Berkelbach, M. S. Hybertsen, D. R. Reichman and T. F. Heinz, *Nat. Phys.*, 2015, **11**, 477–481.
23 Z. Li, T. Wang, Z. Lu, C. Jin, Y. Chen, Y. Meng, Z. Lian, T. Taniguchi, K. Watanabe, S. Zhang, D. Smirnov and S. F. Shi, *Nat. Commun.*, 2018, **9**, 3719.
24 A. Allain and A. Kis, *ACS Nano*, 2014, **8**, 7180–7185.
25 J.-K. Huang, J. Pu, C.-L. Hsu, M.-H. Chiu, Z.-Y. Juang, Y.-H. Chang, W.-H. Chang, Y. Iwasa, T. Takenobu and L.-J. Li, *ACS Nano*, 2014, **8**, 923–930.

26 B. Fallahazad, H. C. Movva, K. Kim, S. Larentis, T. Taniguchi, K. Watanabe, S. K. Banerjee and E. Tutuc, *Phys. Rev. Lett.*, 2016, **116**, 086601.

27 R. Zhao, L. Liu, J. Pei, C. Liu, T. Liu and X. D. Zhang, *Adv. Mater. Interfaces*, 2023, **10**, 2300277.

28 H. Choi, S. Choi, T. Kang, H. Son, C. Kang, E. Hwang and S. Lee, *Adv. Opt. Mater.*, 2022, **10**, 2201196.

29 S. Ghosh, A. Varghese, K. Thakar, S. Dhara and S. Lodha, *Nat. Commun.*, 2021, **12**, 3336.

30 X. Yu, M. S. Prévot, N. Guijarro and K. Sivula, *Nat. Commun.*, 2015, **6**, 7596.

31 Y. Wang, S. Zhao, Y. Wang, D. A. Laleyan, Y. Wu, B. Ouyang, P. Ou, J. Song and Z. Mi, *Nano Energy*, 2018, **51**, 54–60.

32 M. Qorbani, A. Sabbah, Y.-R. Lai, S. Kholimatussadiah, S. Quadir, C.-Y. Huang, I. Shown, Y.-F. Huang, M. Hayashi, K.-H. Chen and L.-C. Chen, *Nat. Commun.*, 2022, **13**, 1256.

33 S. Pakhira, V. Kumar and S. Ghosh, *Adv. Mater. Interfaces*, 2023, **10**, 2202075.

34 S. Lee, C. Fan, T. Wu and S. L. Anderson, *J. Am. Chem. Soc.*, 2004, **126**, 5682–5683.

35 L. Li, Y. Gao, H. Li, Y. Zhao, Y. Pei, Z. Chen and X. C. Zeng, *J. Am. Chem. Soc.*, 2013, **135**, 19336–19346.

36 J. Gao, G. Zhang and Y.-W. Zhang, *J. Am. Chem. Soc.*, 2016, **138**, 4763–4771.

37 Y. Ouyang, Q. Li, L. Shi, C. Ling and J. Wang, *J. Mater. Chem. A*, 2018, **6**, 2289–2294.

38 H. Prats, R. A. Gutiérrez, J. J. Piñero, F. Viñes, S. T. Bromley, P. J. Ramírez, J. A. Rodriguez and F. Illas, *J. Am. Chem. Soc.*, 2019, **141**, 5303–5313.

39 N. Vats, Y. Wang, S. Sen, S. Szilagyi, H. Ochner, S. Abb, M. Burghard, W. Sigle, K. Kern, P. A. van Aken and S. Rauschenbach, *ACS Nano*, 2020, **14**, 4626–4635.

40 J. Lei, X.-X. Fan, T. Liu, P. Xu, Q. Hou, K. Li, R.-M. Yuan, M.-S. Zheng, Q.-F. Dong and J.-J. Chen, *Nat. Commun.*, 2022, **13**, 202.

41 B. Zhang, Y. Chen, J. Wang, H. Pan and W. Sun, *Adv. Funct. Mater.*, 2022, **32**, 2202227.

42 S. Chen, Y. Gao, W. Wang, O. V. Prezhdo and L. Xu, *ACS Nano*, 2023, **17**, 1522–1532.

43 Z. Wu, P. Yang, Q. Li, W. Xiao, Z. Li, G. Xu, F. Liu, B. Jia, T. Ma, S. Feng and L. Wang, *Angew. Chem., Int. Ed.*, 2023, **62**, e202300406.

44 Q. Zhang, Y. Wang, Z. W. Seh, Z. Fu, R. Zhang and Y. Cui, *Nano Lett.*, 2015, **15**, 3780–3786.

45 P. M. Coelho, H.-P. Komsa, H. Coy Diaz, Y. Ma, A. V. Krasheninnikov and M. Batzill, *ACS Nano*, 2018, **12**, 3975–3984.

46 B. Liu, M. Fathi, L. Chen, A. Abbas, Y. Ma and C. Zhou, *ACS Nano*, 2015, **9**, 6119–6127.

47 C. Feng, J. Xiang, P. Liu and B. Xiang, *Mater. Res. Express*, 2017, **4**, 095703.

48 H. Zhu, N. Nayir, T. H. Choudhury, A. Bansal, B. Huet, K. Zhang, A. A. Puretzky, S. Bachu, K. York, T. V. Mc Knight, N. Trainor, A. Oberoi, K. Wang, S. Das, R. A. Makin, S. M. Durbin, S. Huang, N. Alem, V. H. Crespi,

A. C. T. van Duin and J. M. Redwing, *Nat. Nanotechnol.*, 2023, **18**, 1295–1302.

49 R. Yue, Y. Nie, L. A. Walsh, R. Addou, C. Liang, N. Lu, A. T. Barton, H. Zhu, Z. Che, D. Barrera, L. Cheng, P.-R. Cha, Y. J. Chabal, J. W. P. Hsu, J. Kim, M. J. Kim, L. Colombo, R. M. Wallace, K. Cho and C. L. Hinkle, *2D Mater.*, 2017, **4**, 045019.

50 F. Li, Y. Feng, Z. Li, C. Ma, J. Qu, X. Wu, D. Li, X. Zhang, T. Yang, Y. He, H. Li, X. Hu, P. Fan, Y. Chen, B. Zheng, X. Zhu, X. Wang, X. Duan and A. Pan, *Adv. Mater.*, 2019, **31**, e1901351.

51 B. Delley, *J. Chem. Phys.*, 2000, **113**, 7756–7764.

52 J. Zhao, R. Shi, L. Sai, X. Huang and Y. Su, *Mol. Simul.*, 2016, **42**, 809–819.

53 J. P. Perdew, K. Burke and M. Ernzerhof, *Phys. Rev. Lett.*, 1996, **77**, 3865.

54 G. Kresse and J. Furthmüller, *Phys. Rev. B: Condens. Matter Mater. Phys.*, 1996, **54**, 11169.

55 Q. Yuan, J. Gao, H. Shu, J. Zhao, X. Chen and F. Ding, *J. Am. Chem. Soc.*, 2012, **134**, 2970–2975.

56 J. Gao and F. Ding, *Angew. Chem., Int. Ed.*, 2014, **53**, 14031–14035.

57 H. Liu, J. Gao and J. Zhao, *Sci. Rep.*, 2013, **3**, 3238.

58 R. Wu, I. K. Drozdov, S. Eltinge, P. Zahl, S. Ismail-Beigi, I. Božović and A. Gozar, *Nat. Nanotechnol.*, 2018, **14**, 44–49.

59 B. Feng, J. Zhang, Q. Zhong, W. Li, S. Li, H. Li, P. Cheng, S. Meng, L. Chen and K. Wu, *Nat. Chem.*, 2016, **8**, 563–568.

60 J. Zhou, C. Zhu, Y. Zhou, J. Dong, P. Li, Z. Zhang, Z. Wang, Y.-C. Lin, J. Shi and R. Zhang, *Nat. Mater.*, 2023, **22**, 450–458.

61 G. Kresse and D. Joubert, *Phys. Rev. B: Condens. Matter Mater. Phys.*, 1999, **59**, 1758.

62 S. Grimme, J. Antony, S. Ehrlich and H. Krieg, *J. Chem. Phys.*, 2010, **132**, 154104.

63 S. Grimme, S. Ehrlich and L. Goerigk, *J. Comput. Chem.*, 2011, **32**, 1456–1465.

64 H. J. Monkhorst and J. D. Pack, *Phys. Rev. B: Solid State*, 1976, **13**, 5188.

65 G. Henkelman, B. P. Uberuaga and H. Jónsson, *J. Chem. Phys.*, 2000, **113**, 9901–9904.

66 G. Henkelman and H. Jónsson, *J. Chem. Phys.*, 2000, **113**, 9978–9985.

67 G. Henkelman, A. Arnaldsson and H. Jónsson, *Comput. Mater. Sci.*, 2006, **36**, 354–360.

68 J. Tersoff and D. R. Hamann, *Phys. Rev. Lett.*, 1983, **50**, 1998.

69 H. Liu, N. Han and J. Zhao, *RSC Adv.*, 2015, **5**, 17572–17581.

70 S. Zhang, L. Sun, L. Yu, G. Zhai, L. Li, X. Liu and H. Wang, *Small*, 2021, **17**, 2103005.

71 X. Li, G. Jia, J. Du, X. Song, C. Xia, Z. Wei and J. Li, *J. Mater. Chem. C*, 2018, **6**, 10010–10019.

72 Y. Zhang, H. Liu, Y. Zhao, J. Lin, Y. Bai, J. Zhao and J. Gao, *Mater. Horiz.*, 2023, **10**, 2417–2426.

73 X. Zhang, F. Zhang, Y. Wang, D. S. Schulman, T. Zhang, A. Bansal, N. Alem, S. Das, V. H. Crespi, M. Terrones and J. M. Redwing, *ACS Nano*, 2019, **13**, 3341–3352.

74 Y. J. Zheng and S. Y. Quek, arXiv preprint arXiv:1901.05238, 2019.

75 W. Yamaguchi and J. Murakami, *Chem. Phys.*, 2005, **316**, 45–52.

76 S. M. Carrión, R. Pis-Diez and F. Aguilera-Granja, *Eur. Phys. J. D*, 2013, **67**, 3.

77 J. Liu, M. Zeng, L. Wang, Y. Chen, Z. Xing, T. Zhang, Z. Liu, J. Zuo, F. Nan, R. G. Mendes, S. Chen, F. Ren, Q. Wang, M. H. Rummeli and L. Fu, *Small*, 2016, **12**, 5741–5749.

78 C. Bréchignac, P. Cahuzac, N. Kébaïli and J. Leygnier, *J. Chem. Phys.*, 2000, **112**, 10197–10203.

79 Z. Q. Li, J. Z. Yu, K. Ohno, B. L. Gu, R. Czajka, A. Kasuya, Y. Nishina and Y. Kawazoe, *Phys. Rev. B: Condens. Matter Mater. Phys.*, 1995, **52**, 1524–1527.

80 B. Pan, J. Han, J. Yang and S. Yang, *Phys. Rev. B: Condens. Matter Mater. Phys.*, 2000, **62**, 17026.

81 C. Wang, Z. Sun, Y. Zheng and Y. H. Hu, *J. Mater. Chem. A*, 2019, **7**, 865–887.

82 A. Yan, X. Shi, F. Huang, M. Fujitsuka and T. Majima, *Appl. Catal., B*, 2019, **250**, 163–170.

83 D. B. Sulas-Kern, E. M. Miller and J. L. Blackburn, *Energy Environ. Sci.*, 2020, **13**, 2684–2740.

84 F. Chen, T. Ma, T. Zhang, Y. Zhang and H. Huang, *Adv. Mater.*, 2021, **33**, 2005256.

85 Y. Zhang, Y. Xu, J. Guo, X. Zhang, X. Liu, Y. Fu, F. Zhang, C. Ma, Z. Shi, R. Cao and H. Zhang, *Chem. Eng. J.*, 2021, **420**, 129556.

86 Y. Li, L. Yang, H. He, L. Sun, H. Wang, X. Fang, Y. Zhao, D. Zheng, Y. Qi, Z. Li and W. Deng, *Nat. Commun.*, 2022, **13**, 1355.

87 M. Xia, X. Zhao, Y. Zhang, W. Pan and D. Y. C. Leung, *J. Mater. Chem. A*, 2022, **10**, 25380–25405.

88 D. Wang, Z. Zhang, B. Huang, H. Zhang, Z. Huang, M. Liu and X. Duan, *ACS Nano*, 2022, **16**, 1198–1207.

89 Z. Zou, J. Liang, X. Zhang, C. Ma, P. Xu, X. Yang, Z. Zeng, X. Sun, C. Zhu, D. Liang, X. Zhuang, D. Li and A. Pan, *ACS Nano*, 2021, **15**, 10039–10047.